1 **Radiative sensitivity quantified by a new set of radiation flux kernels based**
2 **on the ERA5 reanalysis**

3

4 Han Huang, Yi Huang

5 Department of Atmospheric and Oceanic Sciences, McGill University, Montreal, Canada

6

7

8

9

10

11 Corresponding Authors:

12 Han Huang, han.huang2@mcgill.ca (ORCID: 0000-0002-9143-6453),

13 Yi Huang, yi.huang@mcgill.ca (ORCID: 0000-0002-5065-4198)

14

15

16

17

18 **Abstract**

19

20 Radiative sensitivity, i.e., the response of the radiative flux to climate perturbations, is essential
21 to understanding climate variability. The sensitivity kernels computed by radiative transfer
22 models have been broadly used for assessing the climate forcing and feedbacks in global
23 warming. As these assessments are largely focused on the top of atmosphere (TOA) radiation
24 budget, less attention has been paid to the surface radiation budget or the associated surface
25 radiative sensitivity kernels. Based on the fifth generation European Center for Medium-Range
26 Weather Forecasts atmospheric reanalysis, we produce a new set of radiative kernels for both the
27 TOA and surface radiative fluxes, which is made available at
28 http://dx.doi.org/10.17632/vmg3s67568.1 (H.Huang, 2022). By comparing with other published
29 radiative kernels, we find that the TOA kernels are in agreement in terms of global mean
30 radiative sensitivity and analyzed overall feedback strength. The unexplained residual in the
31 radiation closure tests is found to be generally within 10%, no matter which kernel dataset is
32 used. The inter-kernel bias-induced uncertainty, as measured by the standard deviation of the
33 global mean feedback parameter value, is typically no more than 10% in the longwave and 20%
34 in the shortwave; this uncertainty is much smaller than the inter-climate model spread of the
35 feedbacks. However, there exist more significant regional biases in kernel values, due to the
36 dependence of radiative sensitivity on the atmospheric states, and this contributes to more
37 significant radiation non-closure at the regional scale, such as in the Arctic and Southern Ocean
38 regions. On the other hand, we find relatively larger discrepancies in the surface kernels.
39 Although several kernels can achieve as good radiation closure compared to the TOA kernels,
40 affirming the validity of kernel method for the surface radiation budget analysis, the non-closure
41 residual in certain kernels may amount to over 100% of the total radiation change. The
42 intercomparison of the surface kernels reveals important biases, such as in the radiative
43 sensitivity to air temperature in the lowermost atmospheric layers adjacent to the surface, which
44 is of critical importance to the overall surface feedback strength.

45

46

47

Earth System
Science
Data

Open Access    Discussions

## 1. Introduction

Radiative kernels measure the sensitivity of radiative fluxes to the perturbation of feedback variables, such as temperature, water vapor, albedo and cloud (e.g., Soden & Held, 2006; Y. Huang et al., 2007; Shell et al., 2008; Previdi, 2010; Zelinka et al., 2012; Block & Mauritsen, 2013; Yue et al., 2016; Y. Huang et al., 2017; Pendergrass et al., 2018; Thorsen et al., 2018; Kramer et al., 2019; Smith et al., 2020). Compared to the partial radiative perturbation method (e.g., Wetherald & Manabe, 1988), which is precise but computationally expensive, the kernel method deploys a set of precalculated radiative kernels with simple arithmetic multiplications in feedback quantification and thus is computationally highly efficient, which has greatly facilitated the analysis of radiative feedbacks in global climate models (GCM) (e.g., Soden et al., 2008; Jonko et al., 2012; Vial et al., 2013; M. Zhang & Huang, 2014; Soden & Held, 2006; Dong et al., 2020; Zelinka et al., 2020), as well as in observations (e.g., Dessler, 2010; Kolly & Huang, 2018; B. Zhang et al., 2019; H. Huang et al., 2021). These analyses have helped dissect and understand the climate sensitivity differences among the GCMs, such as those in Coupled Model Intercomparison Projects, CMIP5 (Taylor et al., 2012) and CMIP6 (Eyring et al., 2016). For example, Zelinka et al. (2020) attributed the higher climate sensitivity in the CMIP6 models to their more positive extratropical cloud feedback. The kernel-enabled feedback analyses have also provided insights in the energetics of the climate variations such as the El Nino and Southern Oscillation (ENSO, e.g., Dessler et al., 2010; Kolly & Huang 2018; H.Huang et al. 2021), the Madden-Julian Oscillation (MJO, e.g., B.Zhang et al. 2019) and the Arctic sea ice interannual variability (e.g., Y. Huang et al., 2019), despite the approximation nature of the kernel method and the known limits of its accuracy (e.g., Colman & McAvaney, 1997; H. Huang & Huang, 2021).

Multiple sets of radiative kernels have been developed to date, using different radiation codes and based on different atmospheric state datasets ranging from GCMs to global reanalysis and satellite datasets, for both non-cloud variables (e.g., Soden and Held, 2006; Shell et al., 2008; Huang et al., 2017; Thorsen et al., 2018) and cloud properties (e.g., Zelinka et al., 2012; Yue et al., 2016). As the conventional feedback analyses are mostly concerned with the radiation energy budget change at the TOA, most existing kernels have been developed and tested to address that need, i.e., to measure the feedback contributions to the TOA radiation changes. Although the radiative sensitivity depends on the atmospheric states as well as the radiative transfer codes used to compute the kernel values (e.g., Collins et al., 2006; Y. Huang & Wang, 2019; Pincus et al., 2020), it has been noted that the global mean TOA feedback quantification is insensitive to the used kernel dataset (e.g., Soden et al., 2008; Jonko et al., 2012; Vial et al., 2013). However, as there are increasing interest in regional climate change and associated feedback (e.g., Kolly & Huang, 2016; Huang et al., 2019; Zhang et al. 2019), it becomes important to know how the kernels (dis)agree at regional scales. The generation of the global radiative kernels usually requires radiative transfer computation based on a large number of instantaneous atmospheric profiles. Due to this computational cost, many kernel datasets are generated based on the atmospheric data from an arbitrary calendar year. Given the known interannual climate differences, e.g., between El Niño to La Niña years, this calls into question whether the kernels may differ in important ways for regional feedback assessments.

On the other hand, fewer feedback studies have addressed the surface radiation budget, although its importance has been recognized for such problems as the precipitation change (Previdi, 2010; Pendergrass & Hartmann, 2014; Myhre et al., 2018) and oceanic energy transport

94    (e.g., Zhang & Huang, 2014; Huang et al., 2017). The surface budget analysis requires the use of
95    surface kernels, which are not always available from the published kernel datasets. Few of them
96    have been subject to inter-comparisons or rigorous validation. As explained below in this paper,
97    the computation and use of them require different care than the TOA kernels. Possibly due to the
98    lack of such recognition, there exist considerable discrepancies between the existing surface
99    kernels and some surface budget-centered analyses reported alarmingly large non-closure in their
100    radiation budget analyses (e.g., Vargas Zeppetello et al., 2019), calling into question the validity
101    of kernel method for surface radiation budget analysis. Hence, we are motivated to examine the
102    radiative sensitivity quantified by different kernels, especially for the surface budget.
103         In this work, we produce a new set of radiative kernels for both the TOA and surface
104    radiation fluxes based on the fifth generation European Center for Medium-Range Weather
105    Forecasts atmospheric reanalysis (ERA5, Hersbach et al., 2020), which demonstrates superior
106    accuracy in the quantification of various atmospheric states, and document the key
107    considerations in the kernel computation procedure. We are interested to intercompare the
108    kernels computed from this atmospheric dataset to the other ones, and to investigate the
109    interannual variation of the kernel values due to their atmospheric state dependency. In addition,
110    applying a selected sets of kernels to analyzing the feedback in the CMIP6 models, we
111    investigate how the quantified feedback strength differs in relation to the kernel differences.
112
113

114 **2. Construction of ERA5 radiative kernels**
115
116 **2.1 Radiative transfer model and atmospheric dataset**
117
118         We use the GCM version of the rapid radiative transfer model (RRTMG) (Mlawer et al.,
119    1997) to calculate the radiative kernels. RRTMG conducts radiative transfer calculations in 16
120    longwave (LW) spectral bands and 14 shortwave (SW) bands. The accuracy of this model has
121    been extensively validated against the line-by-line calculations (e.g., Collins et al, 2006).
122         Input data required by RRTMG, including surface pressure, skin temperature, air
123    temperature, water vapor, albedo, ozone concentration, cloud fraction, cloud liquid water content
124    and cloud ice content, are taken from the instantaneous (as opposed to monthly mean) data of the
125    ERA5 reanalysis, with a horizontal resolution of 2.5 degree by 2.5 degree and 37 vertical
126    pressure levels. To ensure the accuracy of radiative kernels in upper atmosphere (Smith et al.,
127    2020), we patch five layers of the U.S. standard profile above 1hPa in the LW calculations. Other
128    required input variables, such as the effective radii of cloud liquid droplet and ice crystal are
129    taken from the 3-hourly synoptic TOA and surface fluxes and cloud product of the Clouds and
130    Earth's Radiant Energy System (CERES) (Doelling et al., 2013). A random cloud overlapping
131    scheme is used in our all-sky calculation. Sensitivity tests have been conducted to determine the
132    necessary temporal sampling for a proper representation of the diurnal cycle and 6-hourly and 3-
133    hourly instantaneous profiles are adopted for LW and SW radiative transfer calculations,
134    respectively, to limit the root mean squared error of the computed diurnal mean flux biases to
135    less than one percent.
136
137

138 **2.2 Radiative kernel computation**
139

140      Radiative kernels in essence measure the change of radiative flux to unit perturbation of
141    atmospheric variables, i.e., $\frac{\partial R}{\partial X}$, where $R$ is either the upwelling irradiance flux at the TOA or
142    downwelling irradiance flux at the surface; $X$ represents the aforementioned feedback variables;
143    $K_X$ is the radiative kernel of variable $X$. Note that for each radiative flux, $K_X$ varies with the time,
144    geographic and vertical locations of the perturbed variable and is in general a 4-dimensional (4-
145    D) data array. Note also that all radiative fluxes and kernel values are defined as downward
146    positive.
147      Following the previous studies, we compute non-cloud radiative kernels including the LW
148    kernels of surface temperature, air temperature, and water vapor, and the SW kernels of surface
149    albedo and water vapor. To calculate the kernels, we use the partial radiative perturbation
150    experiments, conducting two radiative transfer simulations, one without perturbation (control
151    run) and the other with a perturbation of one atmospheric variable. In both experiments, the
152    upward, downward and net radiative fluxes at the TOA and surface are saved at each time
153    instance and location. Then $\Delta R_0$ can be obtained by differencing the saved radiative fluxes
154    between the perturbed and unperturbed experiments. Dividing $\Delta R_0$ with the perturbation of
155    variable $X$ ($\Delta X_0$), the instantaneous radiative kernel $K_X$ is calculated as
156

157                         $$K_X = \frac{\Delta R_0}{\Delta X_0} \qquad (1)$$

158

159      Applying such perturbation computations to all the relevant variables (see Appendix for a
160    detailed discussion of the procedure), we obtain instantaneous radiative kernels of these
161    dimensionalities: the surface temperature and albedo kernels are 3-D arrays (time, latitude|73,
162    longitude|144), and the air temperature and water vapor kernels are 4-D arrays (time, level|37,
163    latitude|73, longitude|144).
164      To account for possible interannual variability of the radiative kernel values, we compute
165    the kernels using atmospheric data of five calendar years: from year 2011 to 2015. Among these
166    years, 2011 is a strong La Niña year, 2015 is a strong El Niño year. Monthly or annual mean
167    kernels are then averaged from the instantaneous computations. For example, the LW annual
168    mean kernels of 2011 is obtained as $K = \frac{1}{365*4}\sum_{i=1}^{365*4} K_i$ and the SW kernels, $K =$
169    $\frac{1}{365*8}\sum_{i=1}^{365*8} K_i$, where the index $i$ represents the time slices included in the averaging. The
170    analyses in this work are based on multi-year mean kernels if not otherwise stated.
171
172
173    **3. Characterization of ERA5 kernels**
174
175      In this section, we first present the radiative sensitivity quantified by the ERA5 kernels and
176    compare them with the other kernel datasets. Then, we examine the interannual variability of the
177    ERA5 kernel values, due to the dependency of radiative sensitivity on the background
178    atmospheric state.
179
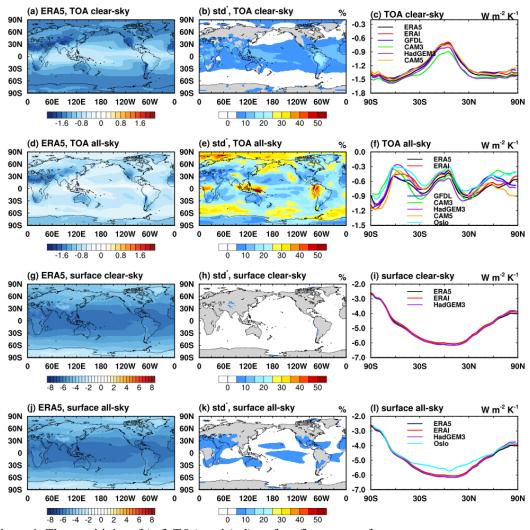180    **3.1 Distribution of radiative sensitivity**
181

182
183   Figure 1. The sensitivity of (a-f) TOA and (g-l) surface fluxes to surface temperature,
184 units: W m$^{-2}$ K$^{-1}$. (a, d, g, j) The annual mean ERA5 sensitivity kernel; (b, e, h, k) the fractional
185 discrepancies, as measured by normalized standard deviation of the kernels listed in the right
186 panel in each raw; (c, f, i, l) zonal mean values of the respective kernels.
187
188   Figure 1 (left column) illustrates the ERA5 surface temperature kernels, i.e., the sensitivity
189 of TOA and surface fluxes to surface temperature. An increase of surface temperature leads to
190 more outgoing longwave radiation (OLR) both at surface and TOA, therefore the kernel is of
191 negative values. The TOA flux sensitivity in clear-sky (Figure 1a) is stronger than that in all-sky
192 (Figure 1d) due to the absence of cloud, and the value increases with latitude, due to the
193 decreasing concentration of water vapor from the tropics to the poles. The all-sky TOA
194 sensitivity is strongly influenced by clouds, showing, for example, the fingerprint of the ITCZ in
195 the tropical oceans. The locations with less atmospheric absorption due to less water vapor or

196    cloud, e.g., in the Tibetan Plateau and Sahara Desert regions, show relatively stronger sensitivity.
197    For the surface flux kernels, the increase of surface temperature enhances the upward emission
198    according to the Planck function and thus the distribution follows that of surface temperature in
199    both clear-sky and all-sky (Figure 1g and j).
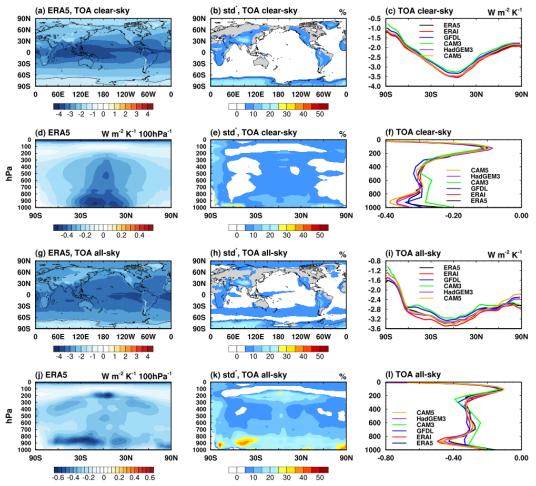200



201
202    Figure 2. The sensitivity of the TOA flux to air temperature, in (a-f) clear-sky and (g-l) all-
203    sky. (a, d, g, j) The annual mean ERA5 kernels, among which (a) and (g) are the vertically
204    integrated sensitivity, units: W m$^{-2}$ K$^{-1}$, and (d) and (j) are the vertically resolved sensitivity,
205    units: W m$^{-2}$ K$^{-1}$ 100hPa$^{-1}$; (b, e, h, k) the fractional discrepancies of the radiative kernels; (c, i)
206    zonal mean vertically integrated radiative kernels, units: W m$^{-2}$ K$^{-1}$; (g, l) global mean vertically
207    resolved kernels, units: W m$^{-2}$ K$^{-1}$ 100hPa$^{-1}$.
208

Open Access Earth System Science Data Discussions
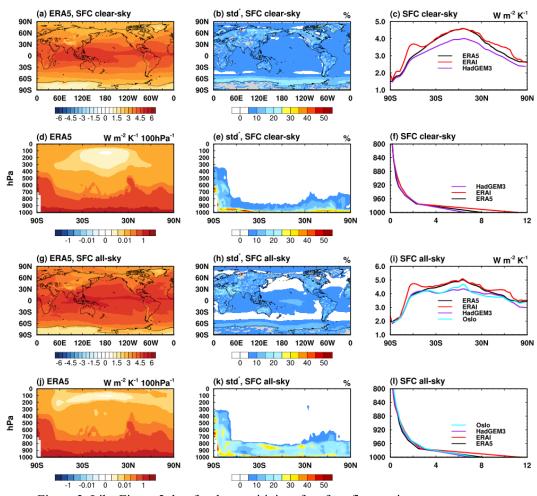


209
210      Figure 3. Like Figure 2, but for the sensitivity of surface flux to air temperature.
211
212          Figures 2 and 3 (left column) show the ERA5 air temperature kernels for TOA and surface
213   fluxes, respectively. The increase of air temperature increases the OLR at TOA and also the
214   downwelling flux at surface, so the TOA and surface kernels take negative and positive signs,
215   respectively. The TOA kernel has maximum values in the tropics, due to the higher air
216   temperature (Planck function) and more abundant cloud and water vapor (higher emissivity)
217   there, and generally decreases in magnitude with latitude. Unlike the TOA flux kernel (Figure
218   2d, j), which shows comparable sensitivity to air temperature at nearly all vertical levels, the
219   surface flux is mainly sensitive to the bottom layers (Figure 3d, j).
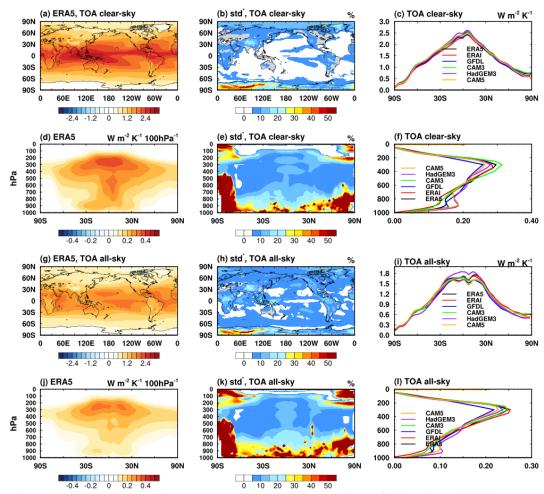
220
221       Figure 4. The sensitivity of the TOA LW flux to water vapor, in (a-f) clear-sky and (g-l)
222 all-sky. (a, d, g, j) The annual mean ERA5 kernels, among which (a) and (g) are the vertically
223 integrated sensitivity, units: W m$^{-2}$ K$^{-1}$, and (d) and (j) are the vertically resolved sensitivity,
224 units: W m$^{-2}$ K$^{-1}$ 100hPa$^{-1}$; (b, e, h, k) the fractional discrepancies of the radiative kernels listed
225 in Table 1; (c, i) zonal mean vertically integrated radiative kernels, units: W m$^{-2}$ K$^{-1}$; (g, l) global
226 mean vertically resolved kernels, units: W m$^{-2}$ K$^{-1}$ 100hPa$^{-1}$.
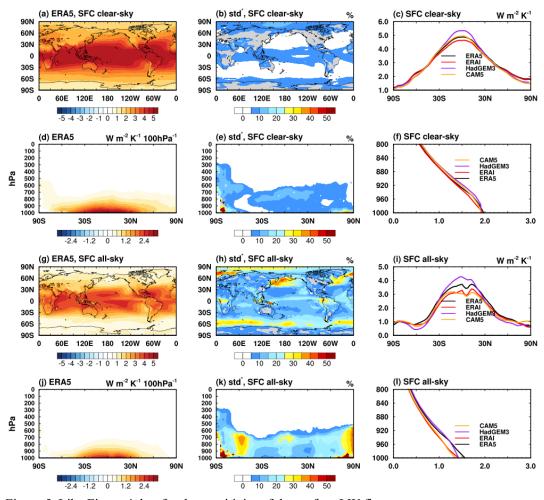227

228
229    Figure 5. Like Figure 4, but for the sensitivity of the surface LW flux to water vapor.
230

231    Figures 4 and 5 (left column) show the ERA5 water vapor LW kernels for TOA and
232 surface fluxes, respectively. An increase of water vapor reduces OLR at TOA and increases
233 downwelling radiation at surface, so that the TOA and surface kernels are both positive in sign.
234 The vertically integrated kernel values (Figure 4a, g and 5a, g) generally follow the temperature
235 distribution, for example, decreasing in magnitude with latitude. In both cases, the kernel
236 magnitude is dampened by clouds in all-sky. The vertically resolved kernels show maximum
237 sensitivity of TOA flux to the upper troposphere (Figure 4d, j) and maximum sensitivity of
238 surface flux to the bottom layers (Figure 5d, j), respectively. Such features were discussed in
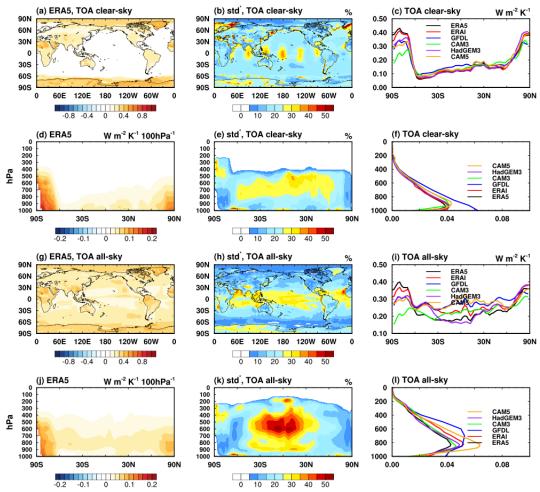239 detail in previous works (e.g., Huang et al. 2007).
240

10

241
242      Figure 6. The sensitivity of the TOA SW flux to water vapor, in (a-f) clear-sky and (g-l)
243 all-sky. (a, d, g, j) The annual mean ERA5 kernels, among which (a) and (g) are the vertically
244 integrated sensitivity, units: W m$^{-2}$ K$^{-1}$, and (d) and (j) are the vertically resolved sensitivity,
245 units: W m$^{-2}$ K$^{-1}$ 100hPa$^{-1}$; (b, e, h, k) the fractional discrepancies of the radiative kernels listed
246 in Table 1; (c, i) zonal mean vertically integrated radiative kernels, units: W m$^{-2}$ K$^{-1}$; (g, l) global
247 mean vertically resolved kernels, units: W m$^{-2}$ K$^{-1}$ 100hPa$^{-1}$.
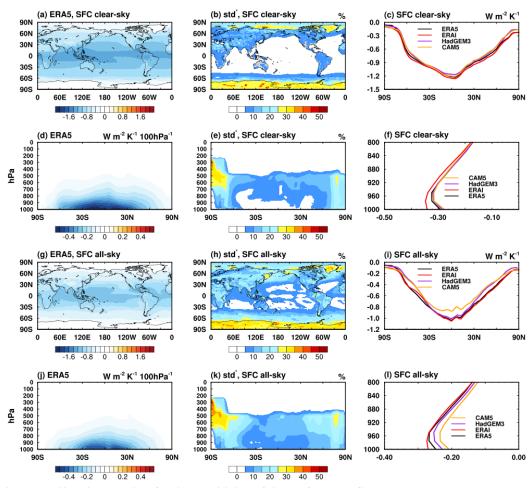248

Figure 7. Like Figure 6, but for the sensitivity of the surface SW flux to water vapor.

Figures 6 and 7 (left column) show the ERA5 water vapor SW kernels for TOA and surface fluxes, respectively. An increase of water vapor absorbs solar radiation and thus reduce both the upwelling (reflected) SW flux at TOA and the downwelling SW flux at surface. As a result, the two kernels take positive and negative signs, respectively. Note the magnitude of the SW kernels is much weaker than that of the LW kernels, because water vapor absorbs the LW flux more significantly than the SW flux. One noticeable feature of the TOA kernel (Figure 6a) is that the magnitude over the land is stronger than that over the ocean, because the relatively higher albedo over the land reflects more SW radiation and thus enhances the absorption by the water vapor in the atmosphere. For this reason, over reflective surfaces such as the Sahara Desert and Tibetan Plateau, as well as the Poles, the sensitivity is maximized. Unlike the TOA kernel, the distribution of surface kernel follows the distribution of background water vapor concentration, with noticeable dampening by clouds (Figure 7a, g).
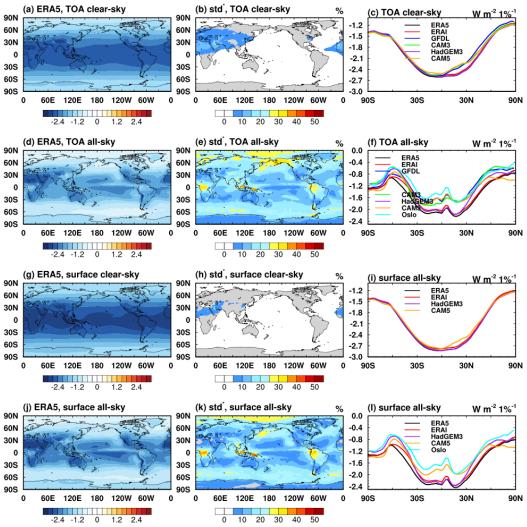
266
267      Figure 8. The sensitivity of (a-f) TOA and (g-l) surface fluxes to surface albedo, units: W
268 m$^{-2}$ 1%$^{-1}$. (a, d, g, j) The annual mean ERA5 sensitivity kernel; (b, e, h, k) the fractional
269 discrepancies of the kernels listed in Table 1; (c, f, i, l) zonal mean of the respective kernels.
270
271      Figure 8 (left column) illustrates the ERA5 surface albedo kernels, i.e., the sensitivity of
272 TOA and surface fluxes to surface albedo. An increase of surface albedo leads to more upwelling
273 (reflected) SW flux both at surface and TOA; therefore, the kernel is of negative sign. In clear-
274 sky, the sensitivity strength follows the pattern of solar insolation, with some local maxima, e.g.,
275 in the Sahara Desert and Tibetan Plateau (Figure 8a, g) due to the relatively lower water vapor
276 concentration. In all-sky, the distribution is again influenced by cloud patterns; for example, in
277 the ITCZ region, the strength is much reduced as clouds reduce the solar radiation reaching the
278 surface and thus the sensitivity to surface albedo change.
279

280
281 **3.2 Comparison of ERA5 kernels with other datasets**
282
283     To examine the discrepancies between different kernel datasets, we select six previously
284 published ones for comparison. Table 1 summarizes their resolutions and the atmospheric
285 datasets based on which they are computed, including the GCMs: GFDL (Soden et al., 2008),
286 CAM3 (Shell et al., 2008), CAM5 (Pendergrass et al., 2018), Oslo (Myhre et al., 2018) and
287 HadGEM3 (Smith et al., 2020) and also a global reanalysis: ERAi (Huang et al., 2017). This list
288 is meant to be representative instead of exhaustive.
289
290     Table 1. Summary of radiative kernels compared in this work. Datasets with * only have
291 TOA kernels. Oslo kernels are only available for all-sky.

| Radiative kernels | Horizontal resolution (lat*lon) | Vertical resolution | Reference |
|---|---|---|---|
| GFDL* | 2x2.5 | 17 (pressure level) | Soden et al., 2008 |
| CAM3* | 2.8x2.8 | 17 (pressure level) | Shell et al., 2008 |
| ERAi | 2.5x2.5 | 24 (pressure level) | Huang et al., 2017 |
| CAM5 | 0.94x1.25 | 30 (hybrid level) or 17 (pressure level) | Pendergrass et al., 2018 |
| Oslo | 2.8x2.8 | 60 (hybrid level) | Myhre et al., 2018 |
| HadGEM3 | 1.25x1.9 | 85 (hybrid level) or 19 (pressure level) | Smith et al., 2020 |
| ERA5 | 2.5x2.5 | 37 (pressure level) | This study |

292
293
294     To facilitate an intercomparison, these kernel datasets are interpolated to the same
295 horizontal and vertical resolutions as those of the ERA5 kernel when illustrated in the middle
296 and right columns in Figures 1 to 8. Note that the CAM5 and HadGEM3 kernels have two
297 versions, with one defined at the raw hybrid levels and the other interpolated to pressure levels.
298 To retain the accuracy of them as much as possible, the hybrid level version is used for the
299 interpolation and comparison in Figures 1-8, while in Section 4, the pressure level version is
300 used for quantifying the feedbacks of CMIP6 models. For the Oslo kernel, only surface
301 temperature, air temperature and surface albedo kernels in all-sky are available and hence it is
302 excluded for clear-sky comparisons. The GFDL and CAM3 kernels are only available for TOA
303 fluxes and are excluded for surface kernel comparisons.
304     Here we use the standard deviation ($std$) and its normalized value ($std^*$) to measure the
305 spread of the inter-kernel dataset biases:

306
$$std_X = \sqrt{\frac{1}{n-1}\sum_{i=1}^{n}\left(K_X^i - \overline{K_X}\right)^2} \quad (2)$$

307
$$std_X^* = \frac{std_X}{\overline{K_X}} * 100 \quad (3)$$

308 where $n$ is the total number of kernel datasets. $K_X^i$ is radiative kernel of variable $X$ from the $i^{th}$
309 dataset. $\overline{K_X}$ is the multi-dataset mean of radiative kernel $K_X$. The distributions of fractional
310 discrepancy ($std^*$) are shown in the middle columns of Figures 1 to 8. Note that some kernels

Earth System
Science
Data

Open Access

Discussions

311    exhibit abnormal values, such as the surface and air temperature kernel of the surface flux in the
312    CAM5 kernel (see Appendix Figure A2) and the air temperature kernel of the TOA flux in the
313    Oslo kernel near the tropopause region (see Appendix Figure A4), indicating inconsistent
314    computation of their values, and thus are excluded in the corresponding $std_X^*$ statistics in Figures
315    1 to 8. See more discussions in Appendix.
316        The comparisons identify the following relatively larger biases in kernel values. Among
317    the TOA kernels, the surface temperature and albedo kernels show relatively large discrepancies
318    in the Arctic, Southern Ocean and over some continental regions in the tropics in all-sky (Figure
319    1e and 8e), with the maximum discrepancy exceeding 30%; the air temperature kernel shows
320    larger discrepancies in the lower troposphere and tropical tropopause region (Figure 2k); these
321    kernel biases are likely due to the differences in cloud fields. The water vapor LW kernel also
322    shows noticeable fractional biases, for example, over the Antarctic region (Figure 4b and h). The
323    water vapor SW kernel shows biases in the tropical mid-troposphere and over Antarctic in both
324    clear-sky and all-sky (Figure 6e and 6k), leading to strong variations in the vertical integration of
325    sensitivity (Figure 6b and 6h), with a spread exceeding 30%. The noticeable periodic equatorial
326    pattern in Figure 6b is caused by the CAM3 kernel, likely due to a coarser temporal resolution
327    that does not well resolve the diurnal cycle of solar insolation in the kernel computation.
328        For the surface kernels, the most prominent biases exist in SW radiative kernels (Figure 7
329    and 8), especially in the polar regions. The discrepancy in the water vapor SW kernel reaches
330    30% for vertically integrated values (Figure 7b and h), with noticeable biases through the
331    troposphere (Figure 7e and k). The surface albedo kernel biases are much larger in all-sky than
332    that in clear-sky, indicating that the cause is in cloud fields, and are also noticeable in the Arctic
333    region due to sea ice variations (Figure 8). In the LW, the water vapor kernels exhibit noticeable
334    biases in the Central Pacific, Southern Ocean and Arctic in all-sky, where again the difference in
335    cloud field is likely the cause. The air temperature kernels show noticeable discrepancies in the
336    bottom layers (Figure 3e), which may be caused by the inconsistency in the kernel computation
337    (see the discussions in Appendix).
338        In summary, the biases among radiative kernel datasets are generally smaller in clear-sky
339    than in all-sky and in most cases, and are largely within 10%. However, there are some notable
340    regional biases, for example, in the surface temperature kernel in the tropics (Figure 1e), in the
341    surface albedo kernel in the Arctic (Figure 8e and k), and in the water vapor SW kernel in the
342    Antarctic region (Figure 7b and h), likely due to the dependence of radiative sensitivity on
343    background climate states, which differ between the kernel datasets. To ascertain the state-
344    dependency caused kernel uncertainty, we next examine the ERA5 kernels computed from
345    different years.
346
347
348    **3.3 Interannual variation of kernel values**
349
350        The intercomparison above identified several prominent inter-dataset biases in the kernel
351    values. For example, there are noticeable differences in the values of surface temperature, albedo
352    and water vapor kernels in the Central Pacific and Arctic region. One possible reason that may
353    account for such differences is the atmospheric state-dependency of the kernel values. Besides
354    the inter-model biases in the different GCM climatology, the interannual variations of the
355    atmospheric states, such as the cloudiness variations in the Central Pacific region during the
356    ENSO cycle, may affect the radiative sensitivity. To test this hypothesis, we use the ENSO and

357 sea ice loss cases to demonstrate the changes in radiative sensitivity with a focus on Central
358 Pacific and Arctic region, respectively. In the ENSO case, the variation is defined as the
359 difference in annual mean kernel values between 2011 and 2015, which have the seasonal sea
360 surface temperature anomalies in the Niño 3.4 region (5N-5S, 190-240E) of -1.4K and +2.6K,
361 respectively. In the sea ice loss case, the variation is calculated as the difference in September
362 between year 2012 and 2013, as the sea ice cover in 2012 was reported to be the lowest level
363 since satellite observation era.
364      To save space, here we only exemplify the most prominent differences. Figure 9
365 summarizes the differences in all-sky for both TOA and surface fluxes due to ENSO. The
366 increases of water vapor concentration and cloudiness in the Central Pacific greatly dampen the
367 sensitivity of OLR to surface temperature change (Figure 9d), with maximum reduction reaching
368 60% (Figure 9d). Also noticed is a weakening of the surface LW sensitivity to water vapor
369 (Figure 9f) and an increase of the TOA SW sensitivity to water vapor (Figure 9e), due to the
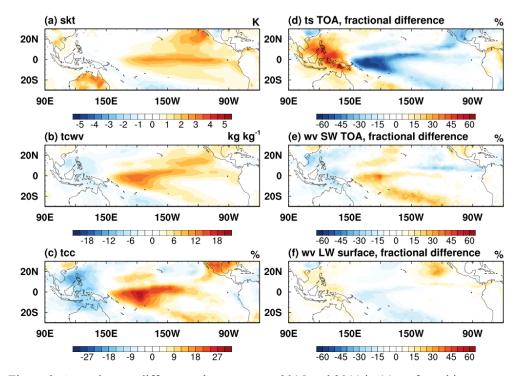370 effects of clouds.
371



372
373      Figure 9. Annual mean differences between year 2015 and 2011 in (a) surface skin
374 temperature, (b) total column water vapor, (c) total cloud cover, and the fractional differences in
375 (d) surface temperature kernel for TOA LW flux, (e) water vapor kernel for TOA SW flux, (f)
376 water vapor kernel for surface LW flux. The fractional difference is quantified relative to multi-
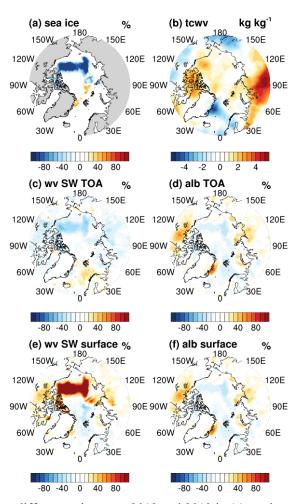377 year mean.
378

379
380    Figure 10. September differences between 2012 and 2013 in (a) sea ice concentration, (b)
381    total column water vapor, and the fractional differences in (c, e) water vapor SW kernel for TOA
382    and surface fluxes, (d, f) surface albedo kernel for TOA and surface fluxes. The fractional
383    difference is measured relative to values in September 2013.
384
385    In the sea ice loss case, the reduction of sea ice in the Arctic region (Figure 10a) leads to a
386    significant decrease of radiative sensitivity to surface albedo (Figure 10d and f), with the
387    maximum difference exceeding 50%, as well as a significant decrease in the TOA sensitivity and
388    an increase of surface sensitivity to water vapor, respectively (Figure 10c and e), with the
389    maximum changes exceeding 80%.
390    In summary, these quantitatively large interannual differences, as well as their locations,
391    which correspond to the inter-dataset kernel differences seen in Figure 1-8, affirm that some
392    discrepancies between the radiative kernels are caused by the difference in atmospheric states.
393    Nevertheless, it ought to be noted that the differences are localized and because of that do not
394    cause significant biases in the global mean feedback values.
395

396
397 **4. Feedback quantification**
398
399      In this section, we apply different kernels to quantifying the radiative feedbacks in one
400 quadrupling $CO_2$ experiment (abrupt4xCO2) of CMIP6 models. This experiment is selected
401 because it has been used by a number of studies for forcing and feedback analyses (e.g., Zelinka
402 et al., 2020), which we can compare our results to. The CMIP6 models used in this assessment
403 are listed in Table2. Note that the standard outputs at 19 pressure levels from the models and
404 correspondingly the kernel values, including CAM5 and HadGEM3, provided at the pressure
405 levels are used in this section.
406
407      Table 2. Summary of CMIP6 models used in this study.

| Models | Horizontal resolution (lat*lon) | Model top level (hPa) | Reference |
| --- | --- | --- | --- |
| CESM2 | 0.9*1.25 | 32 levels to 2.26 hPa | Danabasoglu et al. (2020) |
| CNRM-CM6-1 | 1.4*1.4 | 91 levels to 0.01hPa | Voldoire et al. (2019) |
| EC-Earth3 | 0.7*0.7 | 91 levels to 90 km | Döscher et al. (2022) |
| HadGEM3-GC31-LL | 1.25*1.875 | 85 levels to 85km | Williams et al. (2018) |
| IPSL-CM6A-LR | 1.3*2.5 | 79 levels to 80km | Boucher et al. (2020) |
| MPI-ESM1-2-LR | 1.875*1.875 | 47 levels to 0.01hPa | Mauritsen et al. (2019) |

408
409
410 **4.1 Analysis procedure**
411
412      To quantify the radiative feedbacks, data from two experiments as documented by Eyring
413 et al. (2016) are used: abrupt4xCO2, simulations with an instantaneous quadrupling of $CO_2$
414 concentration of year 1850, piClim-4xCO2, simulations with SST and sea ice concentrations
415 fixed at the climatology of pre-industrial control experiment and $CO_2$ concentration quadrupled.
416 In each experiment, a 20-year period at the end of the simulation in each model is used.
417 Following the previous studies (e.g., Smith et al., 2020; Zelinka et al., 2020), radiative feedbacks
418 are diagnosed using the difference of atmospheric variables between the abrupt4xCO2 and
419 piClim-4xCO2 experiments.
420      To detail the analysis procedure, firstly, all variables including radiative fluxes and
421 atmospheric variables from CMIP6 models are interpolated to the horizontal and vertical
422 resolution of the kernel itself. Notre that for CAM3, GFDL and CAM5 kernels, they only have
423 17 pressure level which are two layers (1hPa and 5hPa) fewer than the CMIP6 standard model
424 output. To address this issue, the contribution of the two missing layers is calculated using other
425 kernels (e.g., ERA5) and found to have negligible effect on the global mean feedback value.
426 Hence, when using these three kernels, the contributions from 10hPa above are ignored.
427      Secondly, the non-cloud radiative feedback of atmospheric variable $X$ is calculated as:
428      $\Delta R_X = K_X \cdot \Delta X$    (4)
429 with units in W m$^{-2}$. For the 2D radiative kernels (surface temperature and surface albedo), $K_X$
430 and $\Delta X$ have just single layer values and $\Delta R_X$ is simply the product of these two terms. For the
431 3D radiative kernels (air temperature and water vapor), both $K_X$ and $\Delta X$ are vectors of pressure

432    levels and $\Delta R_X$ is the dot product of $K_X$ and $\Delta X$. Note that if $K_X$ is normalized with unit pressure
433    thickness (e.g., W m$^{-2}$ K$^{-1}$ 100hPa$^{-1}$), the layer thickness must be taken into account when
434    calculating $dR_X$.
435        Finally, cloud feedbacks are diagnosed using the adjusted cloud-radiative forcing method
436    (Shell et all., 2008). Here we compute the residual term in clear-sky as:
437        $res^o = \sum \Delta R_X^o - \Delta R^o$         (5)
438    and, assuming the all-sky decomposition has the same non-closure residual, the cloud feedback
439    is measured as
440        $\Delta R_c = \Delta R - \sum \Delta R_X + res^o$         (6)
441    where the superscript $o$ represents clear-sky quantities. $\sum \Delta R_X^o$ and $\sum \Delta R_X$ are the sum of non-
442    cloud feedbacks in clear-sky and all-sky, respectively, diagnosed by multiplying the radiative
443    kernel with the atmospheric responses measured as the difference between abrupt4xCO$_2$ and
444    piClim-4xCO$_2$ experiments. $\Delta R^o$ and $\Delta R$ are the total radiation change in clear-sky and all-sky,
445    respectively, calculated as the difference in the GCM-simulated radiative fluxes between two
446    experiments.
447        The feedback parameters, $\lambda_X$, in the units of W m$^{-2}$ K$^{-1}$, are then obtained by normalizing
448    the feedback flux changes $\Delta R_X$ by the global mean surface temperature change $\Delta T_S$ in the
449    abrupt4xCO$_2$ experiment:
450        $\lambda_X = \Delta R_X / \Delta T_S$             (7)
451
452
453    **4.2 TOA feedbacks**
454
455        The residual term ($res^o$) measures the unexplained radiation change in the feedback
456    analysis and provides a useful overall indication of the soundness of the feedback quantification.
457    Figure 11 illustrates the residual term for the TOA flux decomposition when different kernels are
458    used to diagnose the feedback of the HadGEM3-GC3-LL model. Note that the findings described
459    below are insensitive to which GCM is used. In terms of the global mean, all residual terms are
460    of small magnitude, no matter which kernel dataset is used. However, there are some noticeable
461    local residuals, especially for the SW budget, e.g., in the Arctic region and around the Antarctic
462    continent where sea ice changes the most (mid-column in Figure 11). While the non-zero
463    magnitude of the residual is partly due to nonlinearity in the radiation decomposition, e.g.,
464    possible coupling between surface albedo and water vapor (Y. Huang et al., 2021), the spread
465    among the kernel results as evidenced by the line plots of Figure 11 is attributable to the
466    discrepancies in the SW radiative kernels as revealed by the comparisons in Section 3. In the
467    LW, the residual is generally small. In summary, the residual terms for the TOA budget are small
468    in terms of the global mean feedback strengths, affirming the validity of the radiative kernels for
469    feedback quantification.
470        Table 3 summarizes the total feedback parameters quantified by normalizing the total
471    radiative feedback in all-sky (the $\sum \Delta R_X$ term in Equation 6) with the global mean surface
472    temperature change in each model. These results are consistent with other published results. For
473    example, compared with the results of Zelinka et al. (2020) based on the ERAi kernel, the
474    kernel-diagnosed overall feedback parameter in the two results is -0.87 W m$^{-2}$ K$^{-1}$ and -0.85 W
475    m$^{-2}$ K$^{-1}$ for the CNRM-CM6-1 model and -0.81 W m$^{-2}$ K$^{-1}$ and -0.84 W m$^{-2}$ K$^{-1}$ for the
476    HadGEM3-GC3-LL model. The results in Table 3 show that although there are larger local
477    discrepancies, the total feedback strengths diagnosed from different kernels (the 9th rows in

478 Table 3) are in good agreement, with a spread generally within 10%. In comparison, the
479 discrepancy in the overall feedback among different models, even when analyzed by the same
480 kernel dataset (the last column in Table 3), is much larger, amounting to 20% for LW, 70% for
481 SW and 30% for the net. In general, the overall feedback uncertainty as measured by inter-model
482 spread primarily arises from the different climate responses simulated in these models rather than
483 the kernel uncertainty.
484     Table 4 summaries the individual TOA feedback components. For the non-cloud
485 feedbacks in each model analyzed from different kernel datasets (numbers in each column in
486 Table 4), the spreads of LW feedback components are generally within 5%; the spreads in the
487 SW feedback components are within 20%. For the cloud feedbacks, the spreads caused by
488 different kernels are larger. For example, the spread of the LW cloud feedback is 36% in the
489 CESM2 model. The spreads of the SW cloud feedback can exceed 100% in some models. These
490 numbers are consistent with the kernel-induced feedback differences assessed by others (e.g.,
491 Vial et al. 2013). However, it is important to note that these spreads caused by the kernel
492 difference are still less than the inter-GCM spreads of the cloud feedbacks (see the last column of
493 Table 4).
494     In summary, the inter-kernel biases do not lead to significant uncertainty in the analyzed
495 non-cloud feedbacks; although the kernel-induced uncertainty in cloud feedback is larger, this
496 uncertainty is considerably less than the inter-GCM cloud feedback spread.
497
498

Table 3. Kernel-diagnosed all-sky TOA overall feedback parameter of CMIP6 models, units: W m⁻² K⁻¹. The numbers in the brackets of the ERAi kernel row are the results from Zelinka et al. (2020) for comparison. The bolded rows: the mean and standard deviation of the feedback parameter values diagnosed from different kernels for the same GCM; the last column: the mean and standard deviation of the feedback parameter values of different GCMs diagnosed from a same kernel, units: W m⁻² K⁻¹.

| | CESM2 | | | CNRM-CM6-1 | | | EC-Earth3 | | | HadGEM3-GC3-LL | | | IPSL-CM6A-LR | | | MPI-ESM1-2-LR | | | Multi-model mean | | |
|---|---|---|---|---|---|---|---|---|---|---|---|---|---|---|---|---|---|---|---|---|---|
| | LW | SW | Net | LW | SW | Net | LW | SW | Net | LW | SW | Net | LW | SW | Net | LW | SW | Net | LW | SW | Net |
| ERA5 | -1.95 | 1.28 | -0.67 | -1.40 | 0.62 | -0.78 | -1.55 | 0.77 | -0.78 | -2.36 | 1.59 | -0.78 | -1.48 | 0.63 | -0.85 | -1.41 | -0.02 | -1.43 | -1.69±0.39 | 0.81±0.56 | -0.88±0.28 |
| ERAi | -2.01 | 1.27 | -0.74 (-0.64) | -1.46 | 0.61 | -0.85 (-0.87) | -1.61 | 0.76 | -0.85 (-0.89) | -2.42 | 1.57 | -0.84 (-0.81) | -1.55 | 0.62 | -0.93 (-0.97) | -1.48 | -0.03 | -1.51 | -1.75±0.38 | 0.80±0.56 | -0.95±0.28 |
| CAM3 | -1.88 | 1.28 | -0.60 | -1.32 | 0.62 | -0.70 | -1.50 | 0.77 | -0.72 | -2.31 | 1.59 | -0.72 | -1.42 | 0.63 | -0.79 | -1.35 | -0.01 | -1.36 | -1.63±0.39 | 0.81±0.56 | -0.81±0.27 |
| GFDL | -2.04 | 1.28 | -0.76 | -1.50 | 0.61 | -0.90 | -1.65 | 0.75 | -0.90 | -2.46 | 1.57 | -0.89 | -1.60 | 0.62 | -0.98 | -1.55 | -0.02 | -1.57 | -1.80±0.37 | 0.80±0.56 | -1.00±0.29 |
| CAM5 | -1.97 | 1.30 | -0.67 | -1.42 | 0.64 | -0.78 | -1.58 | 0.79 | -0.78 | -2.38 | 1.61 | -0.78 | -1.51 | 0.64 | -0.86 | -1.44 | 0.00 | -1.43 | -1.72±0.38 | 0.83±0.56 | -0.88±0.28 |
| HadGEM3 | -1.92 | 1.26 | -0.65 | -1.39 | 0.61 | -0.78 | -1.55 | 0.77 | -0.78 | -2.35 | 1.58 | -0.77 | -1.47 | 0.62 | -0.85 | -1.40 | -0.03 | -1.43 | -1.68±0.38 | 0.80±0.56 | -0.88±0.28 |
| **Multi-kernel mean** | **-1.96 ±0.06** | **1.28 ±0.01** | **-0.68±0.06** | **-1.42 ± 0.06** | **0.62 ±0.01** | **-0.80 ±0.07** | **-1.57 ±0.05** | **0.77 ±0.01** | **-0.80 ±0.06** | **-2.38 ±0.05** | **1.58 ±0.01** | **-0.79 ±0.06** | **-1.50 ±0.06** | **0.63 ±0.01** | **-0.88 ±0.07** | **-1.44 ±0.07** | **-0.02 ±0.01** | **-1.45 ±0.07** | | | |
| **Multi-kernel λ_res** | **-0.05 ±0.06** | **0.15 ±0.01** | **0.11±0.06** | **0.03 ±0.06** | **0.04 ±0.01** | **0.07 ±0.07** | **0.07 ±0.05** | **0.08 ±0.01** | **0.15 ±0.06** | **-0.06 ±0.05** | **0.04 ±0.01** | **0.02 ±0.06** | **0.00 ±0.06** | **0.03 ±0.01** | **0.03 ±0.07** | **0.09 ±0.07** | **0.04 ±0.01** | **0.13 ±0.07** | | | |
| $dT_s$ (K) | 11.16 | | | 6.59 | | | 7.18 | | | 7.61 | | | 8.24 | | | 4.70 | | | | | |

21

506

507     Table 4. Kernel-diagnosed all-sky TOA radiative feedback parameters, units: W m$^{-2}$ K$^{-1}$.
508 First six columns: the mean and standard deviation of the feedback parameter values diagnosed
509 from different kernels for the same GCM; the last column: the mean and standard deviation of
510 the feedback parameter values of different GCMs diagnosed from multi-kernel mean results,
511 units: W m$^{-2}$ K$^{-1}$.

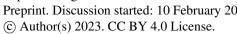|  | CESM2 | CNRM-CM6-1 | EC-Earth3 | HadGEM3-GC3-LL | IPSL-CM6A-LR | MPI-ESM1-2-LR | **Multi-model** |
|---|---|---|---|---|---|---|---|
| $\lambda_{Ts}$ | -0.68±0.02 | -0.65±0.03 | -0.64±0.03 | -0.66±0.03 | -0.63±0.03 | -0.63±0.03 | **-0.65±0.02** |
| $\lambda_{Ta}$ | -3.01±0.05 | -2.92±0.04 | -2.77±0.04 | -3.06±0.04 | -2.83±0.04 | -3.13±0.05 | **-2.95±0.14** |
| $\lambda_q$ LW | 1.60±0.05 | 1.58±0.06 | 1.54±0.05 | 1.51±0.05 | 1.64±0.06 | 1.66±0.06 | **1.59±0.06** |
| $\lambda_c$ LW | 0.13±0.05 | 0.58±0.05 | 0.30±0.04 | -0.17±0.04 | 0.31±0.05 | 0.67±0.05 | **0.30±0.30** |
| $\lambda_q$ SW | 0.25±0.03 | 0.24±0.03 | 0.26±0.03 | 0.24±0.03 | 0.25±0.03 | 0.26±0.03 | **0.25±0.01** |
| $\lambda_{alb}$ | 0.28±0.05 | 0.40±0.07 | 0.44±0.08 | 0.38±0.06 | 0.33±0.05 | 0.32±0.06 | **0.36±0.06** |
| $\lambda_c$ SW | 0.74±0.06 | -0.02±0.07 | 0.07±0.08 | 0.97±0.07 | 0.04±0.06 | -0.59±0.07 | **0.20±0.57** |

512
513

Table 5. Similar to Table 3, but for the surface feedback. The overall feedback parameter and residual term from HadGEM3 kernel are shown in last two rows for comparison.

| | CESM2 | | | CNRM-CM6-1 | | | EC-Earth3 | | | HadGEM3-GC3-LL | | | IPSL-CM6A-LR | | | MPI-ESM1-2-LR | | | Multi-model mean | | |
|---|---|---|---|---|---|---|---|---|---|---|---|---|---|---|---|---|---|---|---|---|---|
| | LW | SW | Net | LW | SW | Net | LW | SW | Net | LW | SW | Net | LW | SW | Net | LW | SW | Net | LW | SW | Net |
| ERA5 | 0.64 | 0.55 | 1.19 | 0.85 | -0.17 | 0.68 | 1.02 | -0.01 | 1.00 | 0.67 | 0.80 | 1.48 | 0.85 | -0.20 | 0.65 | 1.29 | -0.87 | 0.43 | 0.89±0.24 | 0.02±0.60 | 0.90±0.39 |
| ERAi | 0.56 | 0.52 | 1.08 | 0.79 | -0.20 | 0.59 | 0.95 | -0.05 | 0.90 | 0.57 | 0.77 | 1.35 | 0.74 | -0.23 | 0.51 | 1.11 | -0.90 | 0.21 | 0.79±0.22 | -0.01±0.60 | 0.77±0.41 |
| CAM5 | 0.53 | 0.60 | 1.12 | 0.69 | -0.12 | 0.57 | 0.99 | 0.03 | 1.02 | 0.58 | 0.85 | 1.43 | 0.76 | -0.15 | 0.61 | 1.27 | -0.83 | 0.44 | 0.80±0.28 | -0.06±0.60 | 0.87±0.39 |
| Multi-kernel mean | 0.57±0.06 | 0.56±0.04 | 1.13±0.06 | 0.78±0.08 | -0.17±0.04 | 0.61±0.06 | 0.99±0.03 | -0.01±0.04 | 0.98±0.07 | 0.61±0.06 | 0.81±0.04 | 1.42±0.07 | 0.78±0.06 | -0.19±0.04 | 0.59±0.07 | 1.22±0.10 | -0.87±0.04 | 0.36±0.13 | | | |
| Multi-kernel $\lambda_{res}$ | -0.25±0.06 | 0.22±0.04 | -0.03±0.06 | -0.14±0.08 | 0.05±0.04 | -0.19±0.06 | 0.00±0.03 | 0.08±0.04 | 0.08±0.06 | -0.11±0.06 | 0.16±0.04 | 0.05±0.07 | -0.10±0.06 | 0.03±0.04 | -0.13±0.07 | 0.13±0.10 | 0.04±0.03 | 0.18±0.13 | | | |
| HadGEM3 | -2.69 | 0.70 | -1.99 | -2.27 | -0.02 | -2.30 | -2.08 | 0.14 | -1.94 | -2.58 | 0.96 | -1.63 | -2.25 | -0.05 | -2.30 | -1.89 | -0.72 | -2.61 | | | |
| HadGEM3 $\lambda_{res}$ | -3.52 | 0.37 | -3.15 | -3.19 | 0.09 | -3.10 | -3.06 | 0.23 | -2.84 | -3.30 | 0.31 | -2.99 | -3.14 | 0.12 | -3.02 | -2.98 | 0.18 | -2.79 | | | |

522
523        Table 6. Similar to Table 4, but for the surface feedbacks. The temperature feedback
524 parameters from HadGEM3 kernel are shown in last three rows for comparison.
525
526
527

| | CESM2 | CNRM-CM6-1 | EC-Earth3 | HadGEM3-GC3-LL | IPSL-CM6A-LR | MPI-ESM1-2-LR | **Multi-model mean** |
|---|---|---|---|---|---|---|---|
| $\lambda_{Ta} + \lambda_{Ts}$ | -1.14±0.08 | -1.13±0.08 | -1.08±0.06 | -1.07±0.05 | -1.04±0.05 | -0.89±0.00 | **-1.06±0.09** |
| $\lambda_{Ts}$ | -4.00±1.00 | -3.82±0.96 | -3.80±0.96 | -3.96±1.00 | -3.72±0.93 | -3.75±0.95 | **-3.84±0.11** |
| $\lambda_{Ta}$ | 2.87±0.97 | 2.70±0.93 | 2.72±0.91 | 2.89±0.97 | 2.68±0.90 | 2.87±0.94 | **2.79±0.10** |
| $\lambda_q$ LW | 1.99±0.15 | 1.85±0.15 | 2.01±0.15 | 1.92±0.14 | 1.93±0.15 | 2.01±0.15 | **1.95±0.06** |
| $\lambda_c$ LW | -0.28±0.08 | 0.05±0.08 | 0.06±0.09 | -0.24±0.07 | -0.11±0.09 | 0.10±0.10 | **-0.07±0.16** |
| $\lambda_q$ SW | -0.63±0.05 | -0.59±0.06 | -0.63±0.06 | -0.59±0.05 | -0.61±0.06 | -0.64±0.05 | **-0.62±0.02** |
| $\lambda_{alb}$ | 0.34±0.02 | 0.49±0.02 | 0.54±0.02 | 0.46±0.02 | 0.40±0.01 | 0.38±0.03 | **0.44±0.07** |
| $\lambda_c$ SW | 0.84±0.04 | -0.07±0.04 | 0.07±0.04 | 0.95±0.04 | 0.02±0.04 | -0.61±0.05 | **0.20±0.59** |
| | | | | | | | |
| HadGEM3 $\lambda_{Ta} + \lambda_{Ts}$ | -3.86 | -3.70 | -3.66 | -3.76 | -3.60 | -3.54 | |
| HadGEM3 $\lambda_{Ts}$ | -5.12 | -4.89 | -4.86 | -5.06 | -4.74 | -4.79 | |
| HadGEM3 $\lambda_{Ta}$ | 1.26 | 1.19 | 1.20 | 1.29 | 1.15 | 1.26 | |

528
529

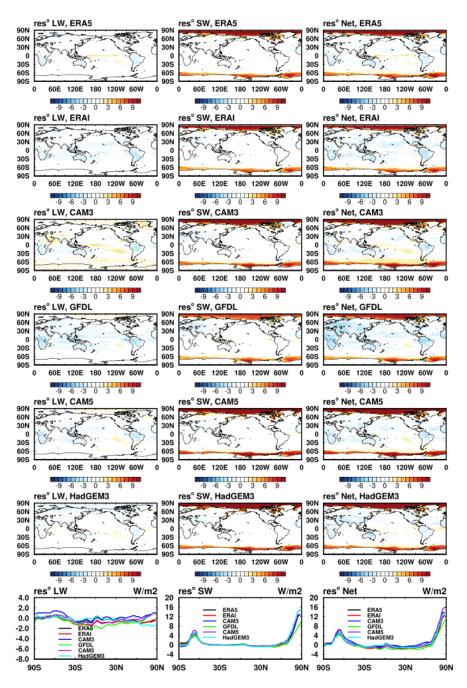Open Access Earth System Science Data Discussions



530
531    Figure 11. The TOA budget residual ($res^o$) in the HadGEM3-GC3-LL model when the
532 feedbacks are calculated by different kernels. (left column) LW, (mid-column) SW, (right-
533 column) Net, the sum of LW and SW. The three line-plots in the bottom row are the zonal mean
534 residuals.

535
536     **4.3 Surface feedbacks**
537
538          Next, we examine how the inter-kernel biases lead to uncertainty in the analyzed surface
539     feedbacks. Figure 12 shows the residual distribution and Table 5 and 6 summarize the global
540     mean feedback strengths.
541          First of all, we find that when the ERA5 and ERAi kernels are used for the feedback
542     analysis, the non-closure residual in the surface budget is comparable in magnitude to the TOA
543     analysis. This suggests that the surface kernels afford a valid tool for the surface feedback
544     analysis. However, some prominent biases are noticed for other kernel datasets. For example, the
545     HadGEM3 kernels, show especially an underestimation in air temperature feedback, likely due to
546     a biased sensitivity of the bottom atmospheric layer (see Appendix for more discussions). The
547     global mean air temperature feedback parameter measured by the HadGEM3 kernel is around
548     1.20 W m$^{-2}$ K$^{-1}$ (compared to around 2.80 W m$^{-2}$ K$^{-1}$ measured by the other kernels), and the
549     non-closure residual is as large as -3.0 W m$^{-2}$ K$^{-1}$ (compared to 0.1 W m$^{-2}$ K$^{-1}$ in the others). For
550     this reason, the result from HadGEM3 kernel is excluded for the multi-kernel statistics in Table
551     5, but listed in a separate row in Tables 5 and 6 for comparison. On the other hand, the results
552     here show that, similar to the TOA assessment, the overall feedback spread across the models
553     (last column in Table 5) is greater than the uncertainty caused by kernel biases.
554          Table 6 lists the individual surface feedback components. For the temperature feedbacks
555     and for the reasons discussed in Appendix, it is advisable to examine the sum of surface and air
556     temperature feedbacks, rather than their separate values as a measure of the inter-kernel biases.
557     For the non-cloud feedbacks, the inter-kernel bias-caused feedback uncertainty is generally
558     within 10%, It is noted that for some feedbacks, such as the water vapor LW and SW feedbacks,
559     the inter-kernel uncertainty exceeds the inter-model uncertainty, which is linked to the large
560     discrepancies detected in the radiative kernel values as shown by Figure 5h and 7h. For the cloud
561     feedbacks, although the kernel-induced uncertainty is higher, with the maximum exceeding
562     100% in some cases, this uncertainty is still less than the inter-model spread of the feedback.
563          In summary, we find the surface feedback decomposition can achieve similar level of
564     radiation closure to the TOA analysis, affirming the validity of kernels for diagnosing the surface
565     radiative feedback. However, the results qualitatively vary depending on which kernel dataset is
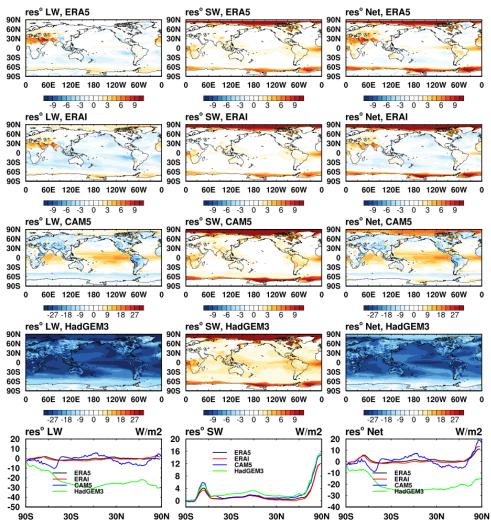566     used, indicating errors in the computation of some kernels.
567
568

Figure 12. Similar to Figure 11, but for the surface feedback analysis.

## 5. Data availability

The datasets contain the multi-year averaged monthly mean TOA and surface kernel for surface temperature, air temperature, surface albedo and water vapor (LW and SW) and are available at: http://dx.doi.org/10.17632/vmg3s67568.1 (H.Huang, 2022).

## 6. Conclusions and discussions

In this paper, we present a newly generated set of ERA5-based radiative kernels of surface and air temperatures, water vapor and surface albedo, and compare them with other

583    published kernels, in terms of the kernel values, as well as the radiative feedbacks quantified
584    from them for both the TOA and surface radiation budgets.

585        For the TOA kernels, the results here affirm general consistency among the different
586    kernel datasets, and the discrepancies are generally within 10% in terms of vertically integrated
587    or globally averaged radiative sensitivity, although some relatively larger regional biases are
588    noticed, including those in the surface temperature kernel in the tropics (Figure 1), those in the
589    surface albedo kernel in the Arctic (Figure 8) and those in the water vapor shortwave kernel in
590    the Antarctica (Figure 6), which is partly due to the dependence of radiative sensitivity on
591    background climate states.

592        For the surface kernels, more prominent inter-kernel biases are found. For example, the
593    biases in the water vapor shortwave kernel in the Antarctic (Figure 7) and in the surface albedo
594    kernel in the Arctic (Figure 8) can reach 30%. It is especially noticed that some kernels have
595    considerably biased air temperature sensitivity values in the bottom atmospheric layers, which is
596    likely due to improper treatment in the perturbation experiments used for kernel computation.
597    The biases in both TOA and surface kernels discovered here affirm the importance of validating
598    the radiative sensitivity as noted by Huang and Wang (2019) and Pincus et al. (2020).

599        Applying the different kernels to quantifying the TOA and surface radiative feedbacks,
600    we compare the feedback differences caused by using different kernels and also the inter-GCM
601    spread of the feedback values (when measured by the same kernel). We find the kernel bias is
602    not a major cause of the inter-GCM feedback spread (Tables 3, 5). This finding is in consistency
603    with the previous assessments (e.g., Soden et al., 2008; Jonko et al., 2012; Vial et al. 2013).

604        Radiation closure tests show that the unexplained residuals are generally within 10% for
605    both TOA and surface analyses in terms of the global mean feedback, affirming the validity of
606    the kernels for feedback quantification for both budgets. This suggests that the large non-closure
607    residuals reported in some previous studies (e.g., Vargas Zeppetello, et al., 2019) are likely due
608    to kernel inaccuracy rather than the limitation of the kernel method. However, there are more
609    significant local non-closures, for example, in the shortwave in the Arctic region and around the
610    Antarctic continent, which is contributed, but cannot be fully explained, by the kernel
611    uncertainty. This points to the accuracy limit of the kernel (linear) method and calls for more
612    advanced methods, such as the neural network method (Zhu et al., 2019), for local feedback
613    analysis.

614

615

616    **Acknowledgements**

617

622

623

624    **References**

625    Block, K., & Mauritsen, T. (2013). Forcing and feedback in the MPI‐ESM‐LR coupled model
626        under abruptly quadrupled CO2. *Journal of Advances in Modeling Earth Systems, 5*(4),
627        676-691.
628    Boucher, O., Servonnat, J., Albright, A. L., Aumont, O., Balkanski, Y., Bastrikov, V., . . . Bopp, L.

629    (2020). Presentation and evaluation of the IPSL‐CM6A‐LR climate model. *Journal of*
630    *Advances in Modeling Earth Systems, 12*(7), e2019MS002010.
631  Collins, W., Ramaswamy, V., Schwarzkopf, M. D., Sun, Y., Portmann, R. W., Fu, Q., . . . Forster,
632    P. (2006). Radiative forcing by well‐mixed greenhouse gases: Estimates from climate
633    models in the Intergovernmental Panel on Climate Change (IPCC) Fourth Assessment
634    Report (AR4). *Journal of Geophysical Research: Atmospheres, 111*(D14).
635  Colman, R., & McAvaney, B. (1997). A study of general circulation model climate feedbacks
636    determined from perturbed sea surface temperature experiments. *Journal of Geophysical*
637    *Research: Atmospheres, 102*(D16), 19383-19402.
638  Danabasoglu, G., Lamarque, J. F., Bacmeister, J., Bailey, D., DuVivier, A., Edwards, J., . . .
639    Gettelman, A. (2020). The community earth system model version 2 (CESM2). *Journal of*
640    *Advances in Modeling Earth Systems, 12*(2), e2019MS001916.
641  Dessler, A. E. (2010). A determination of the cloud feedback from climate variations over the past
642    decade. *Science, 330*(6010), 1523-1527.
643  Doelling, D. R., Loeb, N. G., Keyes, D. F., Nordeen, M. L., Morstad, D., Nguyen, C., . . . Sun, M.
644    (2013). Geostationary enhanced temporal interpolation for CERES flux products. *Journal*
645    *of Atmospheric and Oceanic Technology, 30*(6), 1072-1090.
646  Dong, Y., Armour, K. C., Zelinka, M. D., Proistosescu, C., Battisti, D. S., Zhou, C., & Andrews, T.
647    (2020). Intermodel spread in the pattern effect and its contribution to climate sensitivity in
648    CMIP5 and CMIP6 models. *Journal of climate, 33*(18), 7755-7775.
649  Döscher, R., Acosta, M., Alessandri, A., Anthoni, P., Arsouze, T., Bergman, T., . . . Carver, G.
650    (2022). The EC-Earth3 Earth system model for the Coupled Model Intercomparison
651    Project 6. *Geoscientific Model Development, 15*(7), 2973-3020.
652  Eyring, V., Bony, S., Meehl, G. A., Senior, C. A., Stevens, B., Stouffer, R. J., & Taylor, K. E. (2016).
653    Overview of the Coupled Model Intercomparison Project Phase 6 (CMIP6) experimental
654    design and organization. *Geoscientific Model Development, 9*(5), 1937-1958.
655  Flynn, C. M., & Mauritsen, T. (2020). On the climate sensitivity and historical warming evolution
656    in recent coupled model ensembles. *Atmospheric Chemistry and Physics, 20*(13), 7829-
657    7842.
658  Hersbach, H., Bell, B., Berrisford, P., Hirahara, S., Horányi, A., Muñoz‐Sabater, J., . . . Schepers,
659    D. (2020). The ERA5 global reanalysis. *Quarterly Journal of the Royal Meteorological*
660    *Society, 146*(730), 1999-2049.
661  Huang, H., & Huang, Y. (2021). Nonlinear coupling between longwave radiative climate feedbacks.
662    *Journal of Geophysical Research: Atmospheres, 126*(8), e2020JD033995.
663  Huang, H., Huang, Y., & Hu, Y. (2021). Quantifying the energetic feedbacks in ENSO. *Climate*
664    *Dynamics, 56*(1), 139-153.
665  Huang, Han (2022), "Data for ERA5 radiative kernels", Mendeley Data, V1, [Dataset], doi:
666    10.17632/vmg3s67568.1
667  Huang, Y., Chou, G., Xie, Y., & Soulard, N. (2019). Radiative control of the interannual variability
668    of Arctic sea ice. *Geophysical Research Letters, 46*(16), 9899-9908.
669  Huang, Y., Huang, H., & Shakirova, A. (2021). The nonlinear radiative feedback effects in the
670    Arctic warming. *Frontiers in Earth Science*, 651.
671  Huang, Y., Ramaswamy, V., & Soden, B. (2007). An investigation of the sensitivity of the clear‐
672    sky outgoing longwave radiation to atmospheric temperature and water vapor. *Journal of*
673    *Geophysical Research: Atmospheres, 112*(D5).
674  Huang, Y., & Wang, Y. (2019). How does radiation code accuracy matter? *Journal of Geophysical*

675    *Research: Atmospheres, 124*(20), 10742-10752.
676    Huang, Y., Xia, Y., & Tan, X. (2017). On the pattern of CO2 radiative forcing and poleward energy
677        transport. *Journal of Geophysical Research: Atmospheres, 122*(20), 10,578-510,593.
678    Jonko, A. K., Shell, K. M., Sanderson, B. M., & Danabasoglu, G. (2012). Climate feedbacks in
679        CCSM3 under changing CO 2 forcing. Part I: Adapting the linear radiative kernel technique
680        to feedback calculations for a broad range of forcings. *Journal of climate, 25*(15), 5260-
681        5272.
682    Kolly, A., & Huang, Y. (2018). The radiative feedback during the ENSO cycle: Observations
683        versus models. *Journal of Geophysical Research: Atmospheres, 123*(17), 9097-9108.
684    Kramer, R. J., Matus, A. V., Soden, B. J., & L'Ecuyer, T. S. (2019). Observation‐based radiative
685        kernels from CloudSat/CALIPSO. *Journal of Geophysical Research: Atmospheres,
686        124*(10), 5431-5444.
687    Mauritsen, T., Bader, J., Becker, T., Behrens, J., Bittner, M., Brokopf, R., . . . Esch, M. (2019).
688        Developments in the MPI‐M Earth System Model version 1.2 (MPI‐ESM1. 2) and its
689        response to increasing CO2. *Journal of Advances in Modeling Earth Systems, 11*(4), 998-
690        1038.
691    Mlawer, E. J., Taubman, S. J., Brown, P. D., Iacono, M. J., & Clough, S. A. (1997). Radiative
692        transfer for inhomogeneous atmospheres: RRTM, a validated correlated‐k model for the
693        longwave. *Journal of Geophysical Research: Atmospheres, 102*(D14), 16663-16682.
694    Myhre, G., Kramer, R., Smith, C., Hodnebrog, Ø., Forster, P., Soden, B., . . . Boucher, O. (2018).
695        Quantifying the importance of rapid adjustments for global precipitation changes.
696        *Geophysical Research Letters, 45*(20), 11,399-311,405.
697    Pendergrass, A. G., Conley, A., & Vitt, F. M. (2018). Surface and top-of-atmosphere radiative
698        feedback kernels for CESM-CAM5. *Earth System Science Data, 10*(1), 317-324.
699    Pendergrass, A. G., & Hartmann, D. L. (2014). The atmospheric energy constraint on global-mean
700        precipitation change. *Journal of climate, 27*(2), 757-768.
701    Pincus, R., Buehler, S. A., Brath, M., Crevoisier, C., Jamil, O., Franklin Evans, K., . . . Paynter, D.
702        (2020). Benchmark calculations of radiative forcing by greenhouse gases. *Journal of
703        Geophysical Research: Atmospheres, 125*(23), e2020JD033483.
704    Previdi, M. (2010). Radiative feedbacks on global precipitation. *Environmental Research Letters,
705        5*(2), 025211.
706    Shell, K. M., Kiehl, J. T., & Shields, C. A. (2008). Using the radiative kernel technique to calculate
707        climate feedbacks in NCAR's Community Atmospheric Model. *Journal of climate, 21*(10),
708        2269-2282.
709    Smith, C. J., Kramer, R. J., & Sima, A. (2020). The HadGEM3-GA7. 1 radiative kernel: the
710        importance of a well-resolved stratosphere. *Earth System Science Data, 12*(3), 2157-2168.
711    Soden, B. J., & Held, I. M. (2006). An assessment of climate feedbacks in coupled ocean–
712        atmosphere models. *Journal of climate, 19*(14), 3354-3360.
713    Soden, B. J., Held, I. M., Colman, R., Shell, K. M., Kiehl, J. T., & Shields, C. A. (2008).
714        Quantifying climate feedbacks using radiative kernels. *Journal of climate, 21*(14), 3504-
715        3520.
716    Taylor, K. E., Stouffer, R. J., & Meehl, G. A. (2012). An overview of CMIP5 and the experiment
717        design. *Bulletin of the American meteorological Society, 93*(4), 485-498.
718    Thorsen, T. J., Kato, S., Loeb, N. G., & Rose, F. G. (2018). Observation-based decomposition of
719        radiative perturbations and radiative kernels. *Journal of climate, 31*(24), 10039-10058.
720    Vargas Zeppetello, L., Donohoe, A., & Battisti, D. (2019). Does surface temperature respond to or

721      determine downwelling longwave radiation? *Geophysical Research Letters, 46*(5), 2781-
722      2789.
723 Vial, J., Dufresne, J.-L., & Bony, S. (2013). On the interpretation of inter-model spread in CMIP5
724      climate sensitivity estimates. *Climate Dynamics, 41*(11), 3339-3362.
725 Voldoire, A., Saint‑Martin, D., Sénési, S., Decharme, B., Alias, A., Chevallier, M., . . . Moine,
726      M. P. (2019). Evaluation of CMIP6 deck experiments with CNRM‑CM6‑1. *Journal of*
727      *Advances in Modeling Earth Systems, 11*(7), 2177-2213.
728 Wetherald, R., & Manabe, S. (1988). Cloud feedback processes in a general circulation model.
729      *Journal of the Atmospheric Sciences, 45*(8), 1397-1416.
730 Williams, K., Copsey, D., Blockley, E., Bodas‑Salcedo, A., Calvert, D., Comer, R., . . . Hill, R.
731      (2018). The Met Office global coupled model 3.0 and 3.1 (GC3. 0 and GC3. 1)
732      configurations. *Journal of Advances in Modeling Earth Systems, 10*(2), 357-380.
733 Yue, Q., Kahn, B. H., Fetzer, E. J., Schreier, M., Wong, S., Chen, X., & Huang, X. (2016).
734      Observation-based longwave cloud radiative kernels derived from the A-Train. *Journal of*
735      *climate, 29*(6), 2023-2040.
736 Zelinka, M. D., Klein, S. A., & Hartmann, D. L. (2012). Computing and partitioning cloud
737      feedbacks using cloud property histograms. Part I: Cloud radiative kernels. *Journal of*
738      *climate, 25*(11), 3715-3735.
739 Zelinka, M. D., Myers, T. A., McCoy, D. T., Po‑Chedley, S., Caldwell, P. M., Ceppi, P., . . . Taylor,
740      K. E. (2020). Causes of higher climate sensitivity in CMIP6 models. *Geophysical Research*
741      *Letters, 47*(1), e2019GL085782.
742 Zhang, B., Kramer, R. J., & Soden, B. J. (2019). Radiative feedbacks associated with the Madden–
743      Julian oscillation. *Journal of climate, 32*(20), 7055-7065.
744 Zhang, M., & Huang, Y. (2014). Radiative forcing of quadrupling CO 2. *Journal of climate, 27*(7),
745      2496-2508.
746 Zhu, T., Y. Huang and H. Wei, (2019), Estimating climate feedbacks using a neural network, J.
747      Geophys. Res.-Atmos. doi:10.1029/2018JD029223
748
749
750
751
752

753 **Appendix**
754
755    The ERA5 kernels are computed following Eq. (1) and the approach outlined in Section
756  2.2.
757
758  1. Surface variable kernels
759
760    To execute the partial radiative perturbation computations, the perturbations are prescribed
761  as the following: for the 2D feedback variables, the surface temperature is increased by 1 K and
762  the albedo is increased by 1% at each location. Hence, the units of the two kernels, $K_{Ts}$ and $K_{ALB}$
763  are W/(m$^2$ K)  and W/(m$^2$ 1%), respectively. When applying them to feedback quantification,
764  their feedbacks are quantified as
765    $\Delta R_{Ts} = K_{Ts} \cdot \Delta T_S$    (A1)
766    $\Delta R_{Alb} = K_{ALB} \cdot \Delta Alb$   (A2)
767  where $\Delta T_S$ should be measured in the units of K and $\Delta Alb$ in percent, i.e., the multiply of 1%.
768
769  2. Water vapor kernel
770
771    For the 3D feedback variables, the perturbations are applied to each of the 37 pressure
772  layers (from 1hPa to 1000hPa), one layer at a time and then normalized by the layer thickness.
773  For the water vapor kernel, a 10% incremental perturbation of the water vapor concentration is
774  used. To adapt to the convention used in the majority of the existing kernels, we convert the units
775  of the kernels to represent the radiative flux change corresponding to an increase of water vapor
776  concentration that conserves the relative humidity of the layer under a 1-K increase in air
777  temperature, i.e., converting the units from W/(m$^2$ $\Delta q_0^{+10\%}$ 100hPa)  to W/(m$^2$ $\Delta q_0^{+1K}$ 100hPa):
778    $K_q^{+10\%} = \frac{\Delta R_0}{\Delta q_0^{+10\%}}$     (A3)
779    $K_q^{+1K} = \frac{\Delta R_0}{\Delta q_0^{+1K}} = K_q^{+10\%} \cdot \frac{\Delta q_0^{+10\%}}{\Delta q_0^{+1K}} = K_q^{+10\%} \cdot \frac{\Delta q_0^{+10\%}}{q_0} \cdot \frac{e_s(T_0)}{e_s(T_0+1K)-e_s(T_0)}$     (A4)
780  Where $q_0$ is the unperturbed water vapor concentration, in units of kg kg$^{-1}$. $\Delta q_0^{+10\%}$ is a 10%
781  increment in water vapor concentration. $e_s(T)$ is the saturated water vapor pressure under
782  temperature $T$, and can be measured by empirical formulas; hence,  $\Delta q_0^{+1K}$ can be measured as
783  $q_0[\frac{e_s(T_0+1K)}{e_s(T_0)} - 1]$. Accordingly, when the water vapor kernel is used for water vapor feedback
784  quantification, the feedback is measured as:
785    $\Delta R_q = K_q^{+1K} \cdot \Delta q^{+1K} = K_q^{+1K} \cdot \frac{\Delta q}{\Delta q_0^{+1K}} = K_q^{+1K} \cdot \frac{\Delta q}{q_0} \cdot \frac{e_s(T_0)}{e_s(T_0+1K)-e_s(T_0)}$     (A5)
786  where $\Delta q = q - q_0$ measures the change in water vapor concentration and is normalized by
787  $\Delta q_0^{+1K}$ to give the factor that is multipliable with the $K_q^{+1K}$ kernel value. If using the Clapeyron-
788  Clausius relation, the above expression can be further approximated as
789    $\Delta R_q = K_q^{+1K} \cdot \frac{\Delta q}{q_0} \cdot \frac{e_s}{(de_s/dT) \cdot 1K} = K_q^{+1K} \cdot \frac{\Delta q}{q_0} \cdot \frac{R_v}{L_v} \cdot \frac{T_0^2}{1K}$     (A6)
790  where $R_v$ and $L_v$ are the gas constant and specific latent heat of water vapor, respectively. Note
791  that when the kernels are used, $T_0$ and $q_0$ typically take their values from the base climate
792  appropriate to the application, e.g., the unperturbed climate of a GCM experiment, not
793  necessarily the dataset used for kernel computation.
794

795    3. Air temperature kernel
796
797         For the air temperature kernel, to be consistent with the "inhomogeneous path treatment"
798    that accounts for the vertically non-uniform temperature distribution within each discrete
799    atmospheric layer (Mlawer et al., 1997), perturbations are added not only to the layer-mean
800    temperature but also the temperature at the exiting boundary of radiative fluxes of interest (i.e.,
801    the upper boundary of each layer for the TOA flux and the lower boundary for the surface flux),
802    to appropriately represent the physical temperature perturbation in each layer.
803         A meaningful test to affirm the validity of the air temperature kernel is a vertical sum test,
804    i.e., a linear additivity test to verify the vertical integration of the kernel values reproduce the
805    flux change, either at TOA or surface, in response to a whole-column air temperature increase of
806    1K. Figure A1 shows that the ERA5 kernel well passes this test. However, as shown by Figure
807    12, some kernels (e.g., HadGEM3 kernel) show much weaker radiative response at surface,
808    possibly due to improper treatment of the air temperature perturbation in the kernel computation,
809    which may lead to an underestimated air temperature feedback and large biases in the surface
810    feedback analysis.
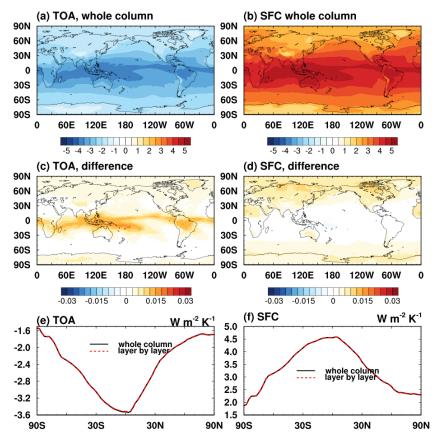811



812
813         Figure A1. Monthly mean TOA and surface radiation flux change in response to a +1K
814    air temperature perturbation throughout the vertical column: (a, b) computed by a radiation

815   model, RRTMG; (c, d) difference of vertical sum of air temperature kernels compared to truth in
816   (a, b); (e, f) comparison of the zonal mean.
817
818       Another trickiness in the computation of air temperature kernel for surface flux is that the
819   surface in radiative transfer models is also the lower boundary of the lowermost atmospheric
820   layer. If the effects of the surface temperature perturbation on the emission of the surface and
821   that of the lowermost atmospheric layer are not distinguished, this may lead to improper
822   interpretation and use of the surface temperature kernel. In our ERA5 kernel, the two effects are
823   considered separately: according to radiative transfer theory, an increase in surface skin
824   temperature only affects the surface upward emission; an increase in air temperature only affects
825   the downward radiation. In some other kernels such as CAM5, these effects are not
826   distinguished, so that the kernel value represents the net effect, i.e., change in the sum of both
827   downward and upward. As a result, in Table 6, we can only report the sum of surface and air
828   temperature feedbacks. Figure A2 shows the comparison of vertically integrated air temperature
829   kernels and the sum of surface and air temperature kernels between ERA5, CAM5 and
830   HadGEM3. Although the strength of vertically integrated air temperature kernel for CAM5 is
831   much weaker than that for ERA5 (Figure A2a and b), the sum of surface and air temperature
832   kernel between these two datasets are in good agreement (Figure A2c and d). Another noticeable
833   feature in Figure A2 is that the HadGEM3 kernel shows an underestimation in vertical
834   integration of air temperature kernel and an overestimation in the sum of surface and air
835   temperature kernel, likely due to mistreatment of the bottom layer and accounting for the biased
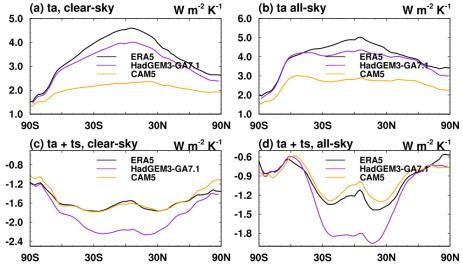836   surface feedback analysis as shown in Figure 12.



837
838       Figure A2. Comparison of annual mean kernels for ERA5, CAM5 and HadGEM3 for (a,
839   b) the vertically integrated air temperature kernel values, and (c, d) sum of surface and air
840   temperature kernels.
841
842
843   4. Time averaging
844

Open Access

Earth System
Science
Data

Discussions

845     As described in Section 2.2, all the kernels provided for feedback analysis are averaged
846 from instantaneous kernel values over each calendar month and, in the ERA5 kernel, over
847 multiple years. This is to ensure proper sampling of radiative sensitivity values under different
848 atmospheric states, so that the kernels are representative of mean radiative sensitivity and thus
849 can be readily multiplied with monthly mean climate responses ($\Delta X$) to evaluate climate
850 feedbacks.
851     If the kernels are computed for fixed pressure levels, and if the pressure of any of these
852 levels of an instantaneous atmospheric profile is higher than the surface pressure (i.e., the level is
853 below the surface) at a time instance, this potentially creates inconsistency in the averaging
854 procedure. To address this concern, we set the kernel value to zero (as opposed to missing value)
855 before averaging. This is to ensure that when multiplied with the monthly mean climate response
856 ($\Delta X$), the contribution of a pressure layer (e.g., that centered at 1000 hPa) is effectively counted
857 only for the fraction of time the layer exists (when surface pressure is higher than 1000 hPa).
858 Otherwise, the feedback quantification needs to be further weighted with fraction of time ($f$)
859 when the pressure layer exists. For example, if the surface pressure is larger than 1000hPa only
860 for half of time in a month ($f=0.5$), the radiation flux anomaly contributed by the layer centered
861 at 1000 hPa is:

862

863     $$\Delta R_{T_{1000hPa}} = K^*_{T_{1000hPa}} \cdot \Delta T_{1000hPa} \cdot f \qquad (A7)$$

864

865 Here, $K^*_{T_{1000hPa}}$ represents the kernel value averaged from the time instances when the layer
866 exists. Our averaging scheme is essentially to provide a kernel $K_{T_{1000hPa}} = K^*_{T_{1000hPa}} \cdot f$, so that
867 it can be simply multiplied with $\Delta T_{1000hPa}$ to obtain the same result.
868     Figure A3 illustrates the differences between $K^*_{T_a}$ and $K_{T_a}$, in terms of their vertically
869 integrated value. Such difference is pronounced over the Southern Oceans (around 60S), where
870 the surface pressure value varies considerably. This likely explains why Figure 3c and i show
871 noticeable differences in the air temperature kernel in this region.
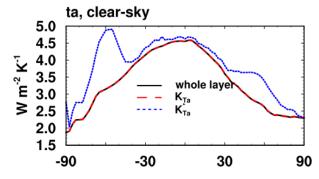


872

873    Figure A3. Zonal mean monthly mean air temperature kernels for surface flux from
874  ERA5 in clear-sky. Black line is the result from the whole column perturbation computation by
875  RRTMG, providing a "truth" for comparison. Red dashed line is the kernel weighted with
876  fraction of time ($K_{T_a}$) and blue dotted line represents results without weights ($K_{T_a}^*$).
877
878  5. Comparison of radiative kernels including all datasets
879
880    Figure A4 shows the comparison of air temperature kernel in all-sky including the Oslo
881  kernel, which compared with Figure 2k and l, shows greater discrepancies above the tropopause
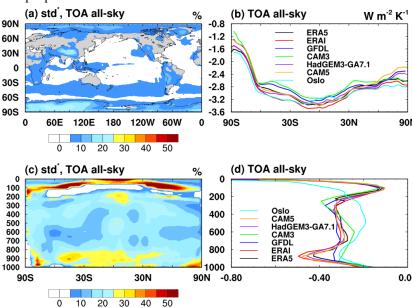882  and in lower troposphere.



883
884    Figure A4. Similar to Figure 2, but including the Oslo kernel in all-sky. (a, c) fractional
885  discrepancies of the radiative kernels; (b) zonal mean vertically integrated radiative kernels,
886  units: W m$^{-2}$ K$^{-1}$; (d) global mean vertically resolved kernels, units: W m$^{-2}$ K$^{-1}$ 100hPa$^{-1}$.
887
888
889
890